THE JOURNAL OF PHYSICAL CHEMISTRY C

Article

Cite This: J. Phys. Chem. C 2018, 122, 14706−14713

pubs.acs.org/JPCC

Atomically-Resolved Oxidative Erosion and Ablation of Basal Plane HOPG Graphite Using Supersonic Beams of O_2 with Scanning Tunneling Microscopy Visualization

Ross Edel,[†] Tim Grabnic,[†] Bryan Wiggins, and S. J. Sibener*

The James Franck Institute and Department of Chemistry, The University of Chicago, 929 East 57th Street, Chicago, Illinois 60637, United States

ABSTRACT: The detailed mechanism and kinetics for the oxidative erosion and ablation of highly oriented pyrolytic graphite (HOPG) with molecular oxygen has been examined by monitoring the spatiotemporal evolution of the reacting interface. This has been accomplished using a new, unique gas-surface scattering instrument that combines a supersonic molecular beam with a scanning tunneling microscope (STM) in ultrahigh vacuum. Using this new instrument, we are able to tightly control the energy, angle, and flux of impinging oxygen along with the surface temperature and examine the reacted surface spanning atomic, nano, and mesocopic length-scales. We observe that different oxidation conditions produce morphologically distinct etching features: anisotropic channels, circular pits, and hexagonal pits faceted along crystallographic directions. These outcomes depend upon independent effects of oxygen energy, incident angle, and surface temperature. Reaction probability increased with beam energy and demonstrated non-Arrhenius behavior with respect to surface temperature, peaking at around 1375 K. At the incident collision energies used, it was found that beam impingement angle had only minor effects on the reaction probability and etch pit morphology. Comparison of the relative reactivity of higher grade versus lower grade HOPG indicates that the formation of etched channels largely depends on the presence of grain boundaries. We have also observed the transition to multilayer etching. The influence of structural inhomogeneities such as defects and grain boundaries can now be assessed by real-time visualization of reacting interfaces. For example, the insertion of intentionally created point defects via ion sputtering leads to marked enhancement in interfacial reactivity. The approach used herein has allowed us to correlate time-evolving surface morphology with atomic-level interfacial kinetics and dynamics, providing new insight into the reactivity of materials in aggressive, energetic environments.

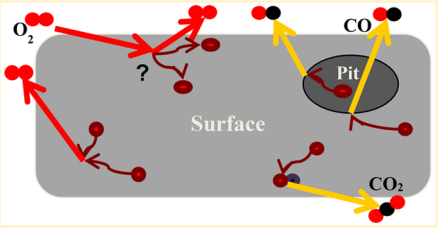

INTRODUCTION

Graphite oxidation is widely studied due to its relevance to technological applications such as high-performance aircraft and propulsion systems and due to its important role as a model system for fundamental studies of materials degradation. The oxidation process with molecular oxygen removes carbon from the surface as the products CO and CO_2, with CO being the dominant reaction product at all surface temperatures[1−4] and impinging oxygen energies.[5−7] Oxygen molecules dissociatively adsorb and diffuse across the surface[8] as adsorbed O before reacting with and removing carbon atoms from the surface. The prismatic plane of HOPG is oxidized much more rapidly than the basal plane, leading to the domination of lateral etching of graphite layers starting from vacancy defects and step edges.[9−13]

In this paper, we present a new approach to studying the dynamics and kinetics of interfacial erosion chemistry where we monitor reactivity not by monitoring CO or CO_2 product formation but rather by visualization of the reacting interface using the combination of supersonic beam scattering coupled with ultrahigh-vacuum scanning tunneling microscopy (STM). This novel approach allows us to directly link the time-evolving morphology of the reacting interface with the observed reaction kinetics, in essence, giving access to the spatiotemporal correlations that govern time-evolving interfacial reactivity. In this instance, visualization encompasses several length-scales including atomic, nano, and mesoscopic distances. The ability to conduct such information-rich experiments was demonstrated for the site-specific energetic oxidation of Si(111)-(7 × 7).[14]

Such spatiotemporal measurements of surface morphological change and surface chemical change directly reveal the key roles that minority structures such as grain boundaries and defects play in determining the time evolution of the interface. This statement, in a broader sense, is especially relevant for intrinsically heterogeneous materials such as functional composites. In this study, we intentionally introduce localized defects using ion sputtering, creating single or multiatom vacancies visible to STM as positive contrast hillocks. These vacancies expose prismatic edge carbons and provide nucleation points for oxidation.[15,16] After a certain induction period, or nucleation phase, the removal of edge carbons results in a visible, negative contrast pit. By providing artificial nucleation points via sputtering, the density of etch features is substantially and controllably increased.

Received: May 1, 2018
Revised: June 2, 2018
Published: June 21, 2018

DOI: 10.1021/acs.jpcc.8b04139
J. Phys. Chem. C 2018, 122, 14706−14713

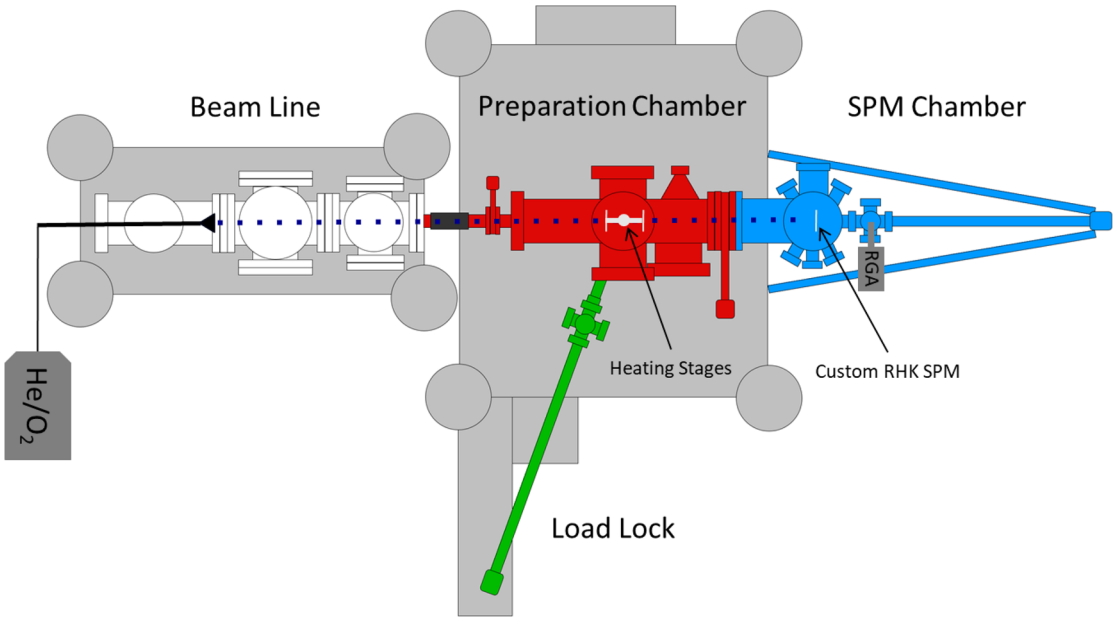

Figure 1. Diagram showing the combined supersonic molecular beam/materials preparation/SPM system.

Previous research has used STM to examine graphite samples etched in furnaces under a high flux of heated molecular oxygen.[9−12,17−22] Circular, monolayer-deep pits were found to arise from these conditions, nucleating exclusively at natural and artificial defects at low temperatures (<1150 K) but nucleating even on the locally perfect (undefected) basal plane at higher temperatures (>1150 K).[12] In some cases elongated, anisotropic channels were observed on furnace-oxidized graphite, but they formed a small minority of features with circular pits dominating.[12,16,23] Pit diameters were found to increase linearly with oxygen exposure, with the lateral etch rate increasing with temperature. The linear growth of pit diameters comports with an overall carbon reaction rate limited by the available density of reactive edge carbons.

At very high temperatures (>1275 K), the overall rate of carbon removal from the surface exhibits apparent non-Arrhenius temperature dependence as a result of the interaction of a number of competing reaction rates. Supersonic beam experiments have determined that peak reactivity occurs at 1400−1500 K, likely due to the increased desorption of adsorbed O atoms at higher temperatures.[5,24−26] An excess of adsorbed O enhances both the formation of new surface vacancies and the etching of existing defects by reducing the barrier to reaction and stabilizing the resulting dangling carbon bonds.[27−29]

More recently, the dependence of etching morphology on surface temperature has been demonstrated, with faceted pits aligned with lattice directions formed below a certain critical temperature, transitioning to circular pits as the temperature was increased.[30] This faceting can be attributed to the preferential reaction of armchair-type edge carbons, leaving only hexagonal pits with zig-zag edges aligned with the <1 1 −2 0 > lattice directions.[31] Although both zig-zag and armchair sites have two neighboring carbon atoms, zig-zag sites have two fully coordinated nearest neighbors, while armchair sites only have one. The higher stability of zig-zag edges thus slightly favors the removal of armchair sites from the surface ($\Delta E_a \approx 0.52$ eV).[30] Above the transition temperature, the reactivity of the two types of edge carbons becomes essentially equivalent, and circular pits result.

EXPERIMENTAL SECTION

These experiments were conducted using a new combined supersonic beam/STM/AFM surface scattering/imaging instrument (Figure 1).[14] It can be viewed as consisting of three sections: the triply differentially pumped beamline, a materials preparation and characterization chamber, and a new variable-temperature SPM that differs from our other SPMs in many critical ways including sample orientation, stability, and thermal equilibration between the tip and sample; it is based on the ultrastable design of Shuheng Pan and has been designed in conjunction with RHK. Most importantly, it has been constructed to allow the surface plane to be vertical, permitting its use in simultaneous or sequential molecular beam plus scanning probe imaging experiments.

Supersonic beams of molecular oxygen were generated by expanding a 5% O_2/95% He gas mixture through a 30 μm diameter molybdenum pinhole at 20 and 70 psi for nozzle temperatures of 300 and 600 K, respectively. The nozzle was heated by resistively heated wire, and the temperature was monitored by a thermocouple. A translational kinetic energy of 0.37 eV with an energy distribution width of $\Delta E/E = 0.28$ was found for the beam with a 300 K nozzle using time-of-flight measurements; the translational kinetic energy of the 600 K beam was extrapolated to be ∼0.7 eV. A flux on the order of 10^{13} O_2 molecules cm^{-2} s^{-1} was determined for both beam conditions. Samples were positioned 1.3 m from the nozzle, with a 2 mm diameter beam spot at the crystal.

HOPG samples were placed in a UHV chamber (base pressure of 1×10^{-10} Torr) in sample mounts that aligned the surface normal either parallel to the beam or at a 45° angle. The sample was maintained at the appropriate temperature (1275−1475 K) during exposure to the supersonic beam of O_2. After exposure, the cooled sample was transferred under vacuum to the STM chamber for imaging.

For these experiments, highly oriented pyrolytic graphite (HOPG, grades SPI-2 and SPI-3) samples were cut into approximately 2 mm × 1 cm strips with a sharp blade and cleaved with adhesive tape. Samples were outgassed in a UHV chamber (base pressure of 1×10^{-10} Torr) up to experimental

DOI: 10.1021/acs.jpcc.8b04139
J. Phys. Chem. C 2018, 122, 14706−14713

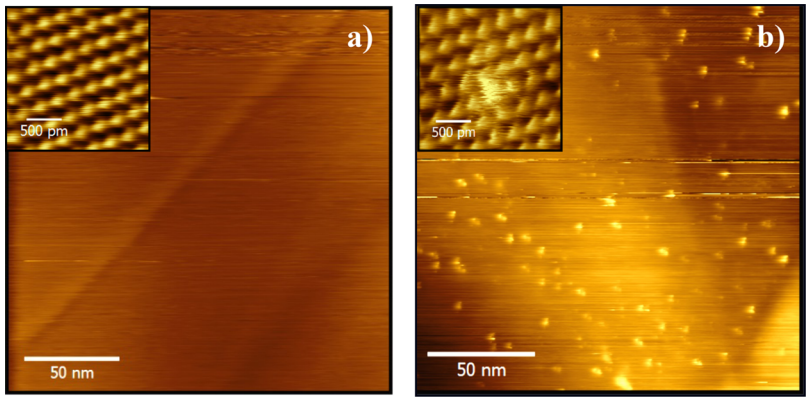

Figure 2. High-resolution STM images. (A) A typical image of the clean basal plane of HOPG with an inset of the clean lattice. (B) A typical sputtered HOPG sample (4 keV Ar^+) with an inset of a single vacancy formed from collision of an Ar^+ ion with the HOPG surface. Images taken at 100 mV and 600 pA.

temperatures (1275−1475 K) prior to exposure. The surface temperature was monitored by a Mikron infrared pyrometer and heated by applying current directly through the sample. Several areas on the surface were checked for cleanliness by STM prior to oxygen exposure. Etched $Pt_{0.8}Ir_{0.2}$ tips were used for imaging. When required, a Phi sputter ion gun was used to create atomic vacancies in the HOPG basal plane by bombarding the sample with 4 keV Ar^+ ions. The 4 keV Ar^+ ions used to prepare our samples induce local point defects most likely consisting of 1−10 removed atoms per created vacancy, this based on prior STM studies.[32] At this scale, the precise atomic-level morphology of the vacancy is obscured by the electronic enhancement resulting from unsaturated dangling bonds.

RESULTS AND DISCUSSION

As the undefected HOPG surface is minimally reactive, defects were introduced by sputtering. Figure 2 shows an unsputtered and unreacted basal plane of HOPG as well as a surface that was sputtered to induce surface vacancies. The average surface density of reactive defects after sputtering was $7 \times 10^9 \pm 1 \times 10^9$ cm^{-2}. Sputter defects serve as nucleation points, leading to a higher density of etch features. In addition, the defects shorten the nucleation phase, defined as the period of time (exposure) that transpires before visible etch pits are formed. In the case of a sputtered surface, a certain number of atoms must be removed from around the initial vacancy before it is imaged by STM as a depression rather than a hillock. A longer nucleation phase is observed on a clean basal surface in comparison to an artificially defected surface as a result of the amount of exposure necessary for a very low probability event, the abstraction of a fully coordinated basal carbon atom, to occur before this transition from hillocks to pits can commence. As seen in Figure 3, the nucleation phase of a sputtered sample is reduced by half as compared to an unsputtered sample. While nucleation was observed predominantly at sputter defects at a surface temperature of 1275 K, at higher surface temperatures, pit formation was observed on the undefected portions of the surface that remained after all initial nucleation points had been consumed. This vertical etching has a higher energetic barrier than lateral etching (E_a = 2.00 eV compared to E_a = 1.48 eV for the latter),[10] because it requires the removal of a carbon atom from an undefected basal plane. Therefore, it only emerges at higher surface temperatures and occurs much more slowly.

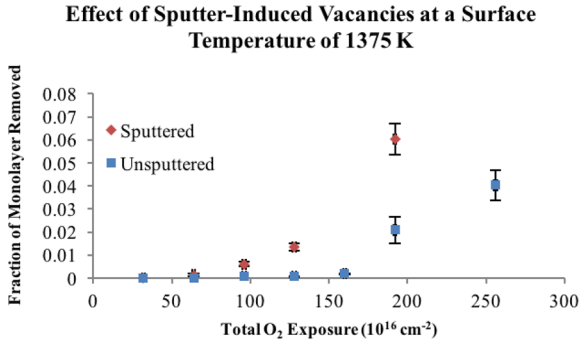

Figure 3. Effect of sputter-induced vacancies on the nucleation phase of a 1375 K HOPG surface exposed to an effusive distribution of background O_2 at 1×10^{-6} Torr.

Along with changes in the overall kinetics of carbon removal from the surface, the surface temperature also affects the morphology of etch pits. Below surface temperatures of ∼1325 K, etch pits formed on the surface by exposure to 0.4 eV oxygen were hexagonal. Computational and experimental studies have demonstrated that lower surface temperature etching forms hexagonal pits on the surface due to small energetic differences between removing a zig-zag and an armchair carbon atom.[30] Consequently, armchair sites will etch at a higher rate than zig-zag sites, leading to the formation of hexagonal pits with zig-zag edges, as seen in Figure 4a. Figure 4b demonstrates the difference between zig-zag and armchair sites on the HOPG honeycomb lattice, while Figure 4c is a schematic representing the sequential removal of zig-zag and armchair carbon atoms during the growth of a hexagonal pit. Note that the STM only images every other basal carbon atom in the full honeycomb lattice (namely, out of the α and β atoms contained in each unit cell, only the β atom is detected), as seen in Figure 4c and the inset of 4a.[33]

At a higher surface temperature of 1375 K, circular, monolayer pits form on the surface when exposed to 0.4 eV O_2. This suggests that the surface has enough energy to overwhelm any small energetic differences between armchair and zig-zag sites, which results in the two sites etching at approximately the same rate. This leads to the formation of circular pits, as seen in Figure 5. A similar transition was found in previous work under different experimental conditions.[30] As would be expected, the creation of circular etch pits was observed at the higher surface temperature of 1475 K when exposed to 0.4 eV

DOI: 10.1021/acs.jpcc.8b04139
J. Phys. Chem. C 2018, 122, 14706−14713

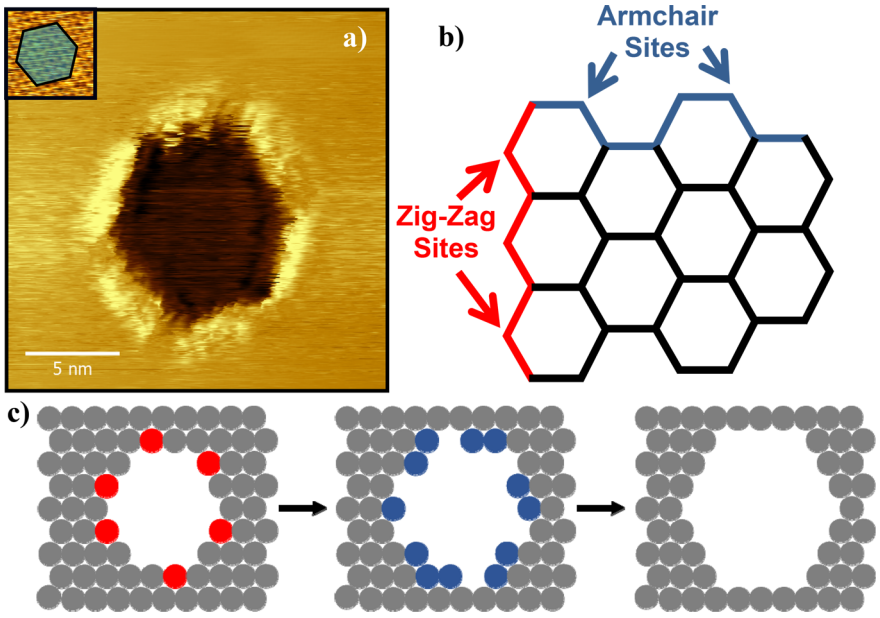

Figure 4. (A) STM image of a representative etch pit formed on a sputtered HOPG sample after exposure to 0.4 eV O_2 at a surface temperature of 1275 K, with the inset showing a lattice aligned with pit edges. Set point: 1.1 V, 600 pA. (B) Skeleton diagram of the HOPG basal plane demonstrating the difference between zig-zag (red) and armchair (blue) sites. (C) Schematic representation of the formation of hexagonal pits through preferential etching of armchair (blue) over zig-zag (red) carbon atoms. The diagram represents the lattice as imaged by STM, as seen in the inset of (A).[33]

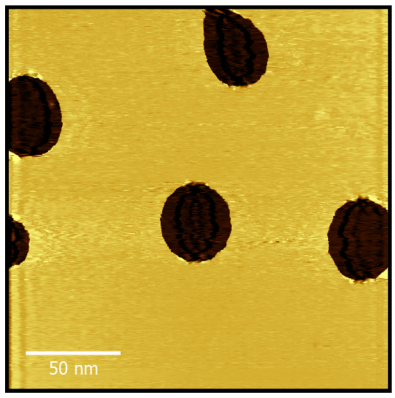

Figure 5. STM image of representative etch pits formed on a sputtered HOPG sample after exposure to 0.4 eV O_2 at a surface temperature of 1375 K. Set point: 300 mV and 600 pA.

O_2, although these pits grew at a much slower rate than those on a 1375 K surface.

Previous work with samples reacted in tube furnaces has demonstrated the diameter of etch pits growing linearly with exposure,[9−12] indicating that the total rate of carbon removal increases with O_2 exposure. This suggests that the surface becomes more reactive as etch features grow and edge carbons with unsaturated dangling bonds become more pervasive.

Interestingly, under all conditions examined here, the rate of carbon removal was constant with oxygen exposure, with no increase due to the proliferation of edge carbons. This suggests that O_2 can adsorb at an arbitrary location and diffuse across the surface as adsorbed O to find a reactive edge carbon, such that the rate-limiting step of carbon removal from the surface is not sensitive to the density of edge carbons (as in the high O_2 flux conditions of previous experiments) but instead is dependent on the concentration of oxygen adsorbed on the surface. Figure 6 demonstrates the constant rate of carbon removal on an HOPG surface at temperatures of 1275, 1375, and 1475 K. The slope of each linear fit corresponds to the probability of a given O_2 molecule removing a carbon atom from the surface. For 0.4 eV O_2 molecules, the values of these reaction probabilities are $3 \times 10^{-6} \pm 1 \times 10^{-6}$, $2 \times 10^{-4} \pm 1 \times 10^{-4}$, and $7 \times 10^{-6} \pm 3 \times 10^{-6}$ for surface temperatures of 1275, 1375, and 1475 K, respectively. Previous studies on graphite oxidation have demonstrated non-Arrhenius behavior with respect to surface temperature, and our findings exhibit similar behavior.[5,26] Our experiments in the 1275−1475 K surface temperature range reached a maximum reaction probability at ~1375 K, which agrees well with previously reported values. This behavior is likely due to decreasing coverage of adsorbed O atoms with increased temperature.[24,25] The effect of oxygen energy on reactivity in the initial oxidation regime is clear in the normally oriented beam experiments: when the beam energy was raised from 0.4 to 0.7 eV, the overall reactivity of the surface increased significantly for both the 1275 and 1375 K surfaces. The reaction probability of impinging 0.7 eV O_2 is $4 \times 10^{-4} \pm 2 \times 10^{-4}$ and $5 \times 10^{-4} \pm 2 \times 10^{-4}$ for surface temperatures of 1275 and 1375 K, respectively; this corresponds to an increase of a factor of over 100 for the 1275 K surface and of over 2 for the 1375 K surface, as seen in Table 1.

In addition to increasing the reaction probability of impinging oxygen, raising the incident O_2 energy from 0.4 to 0.7 eV drastically changes the morphology of the etch features on the surface. The 0.4 eV O_2 predominantly created symmetrical etch pits, with hexagonal pits formed at lower surface temperatures (<1325 K) and circular pits formed at higher surface temperatures. By contrast, at the higher beam energy of 0.7 eV, irregular, anisotropic etch channels dominated, as seen in Figure 7. This channeling phenomenon was observed at surface temperatures of both 1275 and 1375 K, indicating that it is caused solely by the impinging oxygen energy. New pits appeared to remain mostly symmetrical up to a maximum radius of about 20 nm, by which point they

DOI: 10.1021/acs.jpcc.8b04139
J. Phys. Chem. C 2018, 122, 14706−14713

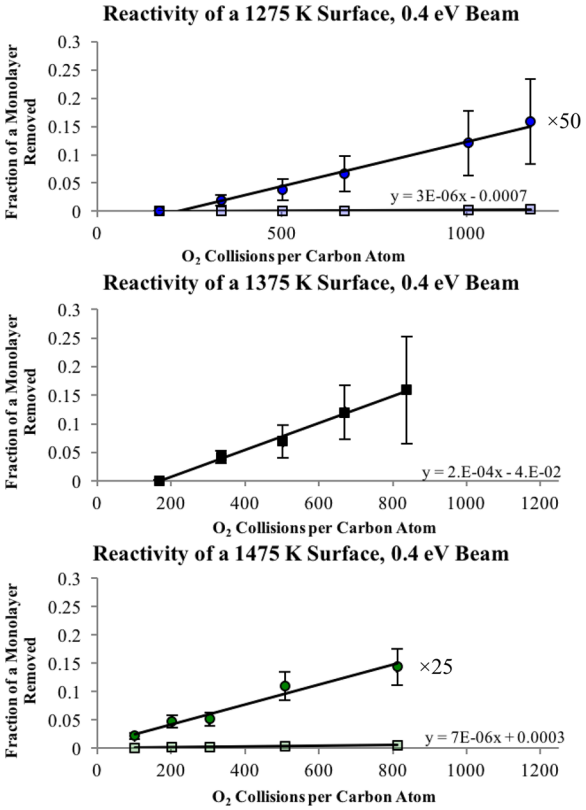

Figure 6. Reactivity plots of 1275 K (top), 1375 K (middle), and 1475 K (bottom) HOPG surfaces exposed to 0.4 eV O_2, where the fraction of the surface monolayer reacted is plotted against the average number of collisions an individual carbon atom has with O_2 molecules. The linear fit to each of these plots corresponds to the probability of an O_2 molecule ultimately removing a carbon atom from the surface. The reactivity plots for the 1275 and 1475 K surfaces are magnified by 50 and 25 times, respectively, to be visible on the same scale as the plot for the 1375 K surface.

spawned rapidly growing channels. The morphology of the pits prior to channeling was similar to those in the 0.4 eV experiments, although the 1275 K surface also formed unusual, nearly triangular pits in some areas (as shown in Figure 7a), which may result from locally decreased surface temperatures.[34]

It is interesting to note that the reaction probabilities with 0.7 eV O_2 at both surface temperatures are roughly equal, suggesting that the large influence of surface temperature over carbon removal rate seen with 0.4 eV oxygen is specific to the formation of circular and hexagonal pits. The enhancement to the reaction probability at both surface temperatures at the higher beam energy can be attributed to the new anisotropic channeling mode that emerges, which is evidently not dependent on surface temperature and dominates over the symmetrical pit etching mode. The etching process giving rise to these channels is thus kinetically as well as morphologically distinct.

The observed increase in carbon removal rate is unlikely to stem from a direct abstraction mechanism, whereby by the O_2 molecule removes a carbon atom from the surface through direct collision to form CO_2. Studies on systems with much higher incident O_2 energies suggest that there is no available reaction mechanism by which an O_2 molecule will directly abstract a carbon atom from the surface; the energy required is too great to render this a realistic possibility. Instead, computational and experimental findings demonstrate that O_2 does not chemisorb as molecular oxygen but rather undergoes exothermic dissociative chemisorption, forming adsorbed O atoms.[16]

Results on higher grade HOPG samples indicate that channels may be following domain boundaries, explaining their irregular, elongated shape. Channels attributed to grain boundaries have been observed previously, although on a larger micron scale and under different conditions.[35,36] On lower grade HOPG (SPI-3) with lateral grains no larger than 30−40 nm, most pits remain roughly circular up to an ∼20 nm diameter before channeling. By contrast, on higher grade samples (SPI-2) with lateral grain sizes of 0.5−1.0 mm, only circular pits are found after exposure to 0.7 eV at a surface temperature of 1375 K, as seen in Figure 8. This result suggests that intrinsic surface properties dictate channel morphology, as the only significant reactive difference between the two samples is the difference in lateral grain sizes. Due to the absence of channeling, the reaction probability of 0.7 eV O_2 on a 1375 K surface drops from $5 \times 10^{-4} \pm 2 \times 10^{-4}$ on an SPI-3 HOPG surface to $3 \times 10^{-5} \pm 1 \times 10^{-5}$ on an SPI-2 HOPG surface, decreasing by over an order of magnitude. This once again demonstrates the connection between kinetics and morphology: the channeling process must be fundamentally faster than pit formation, and thus, when the surface structure is not conducive to channeling, the kinetic enhancement of 0.7 eV oxygen fails to materialize.

The relationship between vertical etching rates on 1275 and 1375 K surfaces remained relatively unchanged with an increase in beam energy from 0.4 to 0.7 eV. On a 1375 K surface, large, two-layer etch features were observed after approximately 20% of the surface monolayer was removed, indicating that new etch features were nucleated on the clean second layer after it was unearthed. Additional multilayer features up to over 20 layers deep (Figure 9) were observed on the 1375 K sample after an O_2 exposure of approximately 4×10^{18} cm^{-2}. In contrast, only limited two-layer etch features were observed on the 1275 K HOPG sample, even when about 30% of the surface monolayer was removed, and no etch features over two layers deep were observed. Thus, as with

Table 1. Complete List of O_2 Reaction Probabilities for All Sets of Experimental Conditions

translational O_2 energy (eV)	HOPG grade	impinging O_2 angle (deg)	surface temperature (K)	reaction probability
0.4	SPI-3	90	1275	$3 \times 10^{-6} \pm 1 \times 10^{-6}$
0.4	SPI-3	90	1375	$2 \times 10^{-4} \pm 1 \times 10^{-4}$
0.4	SPI-3	90	1475	$7 \times 10^{-6} \pm 3 \times 10^{-6}$
0.4	SPI-3	45	1375	$1.1 \times 10^{-4} \pm 5 \times 10^{-5}$
0.7	SPI-3	90	1275	$4 \times 10^{-4} \pm 2 \times 10^{-4}$
0.7	SPI-3	90	1375	$5 \times 10^{-4} \pm 2 \times 10^{-4}$
0.7	SPI-2	90	1375	$3 \times 10^{-5} \pm 1 \times 10^{-5}$
0.7	SPI-2	45	1375	$3 \times 10^{-5} \pm 1 \times 10^{-5}$

DOI: 10.1021/acs.jpcc.8b04139
J. Phys. Chem. C 2018, 122, 14706−14713

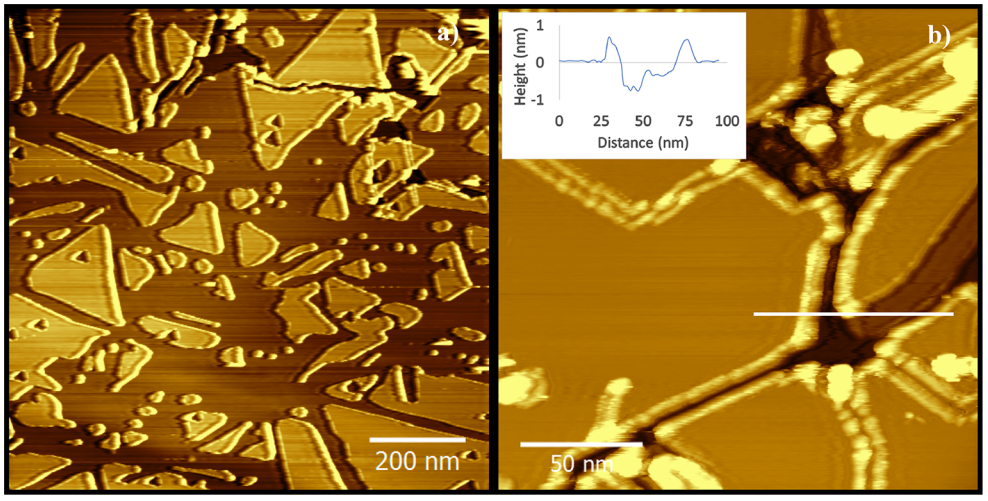

Figure 7. STM images of representative etch channels formed on a sputtered HOPG sample after exposure to 0.7 eV O_2 at a surface temperature of (A) 1275 K (400 mV, 700 pA) and (B) 1375 K (300 mV, 600 pA); the inset line scan represents areas of single and double layer etching, with two negative contrast terraces at around 0.3 and 0.8 nm corresponding to one- and two-layer-deep etch features, respectively. Multilayer etch features are much more abundant on a 1375 K surface in comparison to a 1275 K surface due to increased vertical etching. For example, multilayer etching was more pervasive on the surface shown in (B) despite it being exposed to about 1/3 as much O_2 as the surface in (A). Faceted etch pits up to ~20 nm in diameter were also observed on the 1275 K surface as seen in (A).

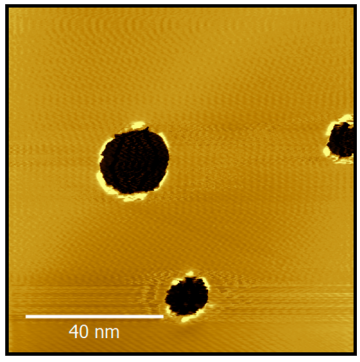

Figure 8. STM image of representative etch pits formed on a sputtered SPI-2 HOPG sample after exposure to 0.7 eV O_2 at a surface temperature of 1375 K. Set point: 300 mV and 700 pA.

0.4 eV oxygen, the increase in surface temperature allows new pits to nucleate on undefected graphite after the consumption of all initial surface defects. This suggests that the abstraction of carbon from the basal plane is limited by surface temperature and not dependent on incident O_2 energy.

Experiments conducted with an impinging O_2 angle of 45° from the surface normal with 1375 K surfaces suggest that the impact angle of O_2 may affect etch feature morphology, while the total overall reactivity of the surface remains relatively unchanged. Exposure of 0.4 eV O_2 to an SPI-3 1375 K surface at 45° found a negligible decrease in overall reactivity to $1.1 \times 10^{-4} \pm 5 \times 10^{-5}$ compared to $2 \times 10^{-4} \pm 1 \times 10^{-4}$ with the beam directed normal to the surface. Etch pits were mostly circular as in the normal-angle case. Results from a SPI-2 surface heated to 1375 K and exposed to 0.7 eV O_2 at 45°

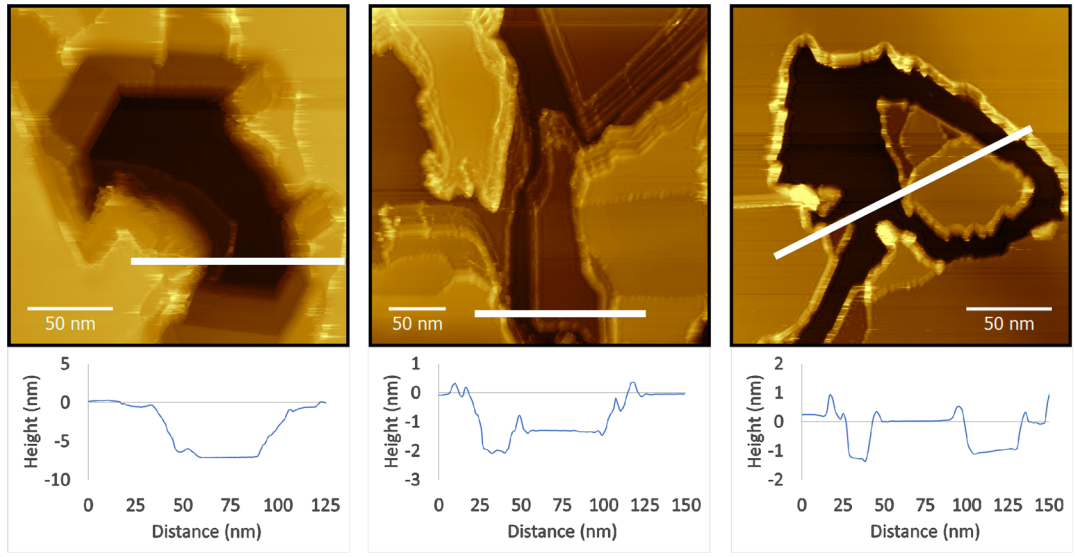

Figure 9. STM images of multilayer (tens of layers deep) etch pits formed on a sputtered SPI-3 HOPG sample after exposure to 0.7 eV O_2 at a surface temperature of 1375 K. Images taken at 300 mV, 700 pA; 100 mA, 700 pA; and 100 mA, 700 pA respectively.

DOI: 10.1021/acs.jpcc.8b04139
J. Phys. Chem. C 2018, 122, 14706−14713

indicate that O_2 impinging at that angle may form different etch features than normal-angle O_2. The exposed surface was dominated by the formation of faceted, monolayer-deep etch pits, shown in Figure 10a, in contrast to the circular pits found with 0.7 eV O_2 normal to a SPI-2 surface. However, more temperature-dependent studies are needed to conclusively say if and how the impingement angle affects the faceted to circular morphological transition. Interestingly, large elongated pits often nucleated on intrinsic linear defects, as shown in Figure 10b. While these lines clearly serve as nucleation sites and likely cause the pit elongation by facilitating etching along the defect, they do not form narrow channels like those found on a SPI-3 surface exposed to 0.7 eV oxygen. The measured overall reaction probability with a 1375 K SPI-2 surface exposed to 0.7 eV O_2 at a 45° impingement angle is $3 \times 10^{-5} \pm 1 \times 10^{-5}$, approximately the same as the normal-angle experiment ($3 \times 10^{-5} \pm 1 \times 10^{-5}$) despite the $\sqrt{2}$ decrease in O_2 translational energy perpendicular the surface. The emergence of faceted pits at a more glancing angle might indicate slight changes in site-selective reactivity, but these differences did not cause a significant change in the overall rate of carbon removal from the surface. More studies need to be completed to determine the mechanistic differences between O_2 impinging at various angles.

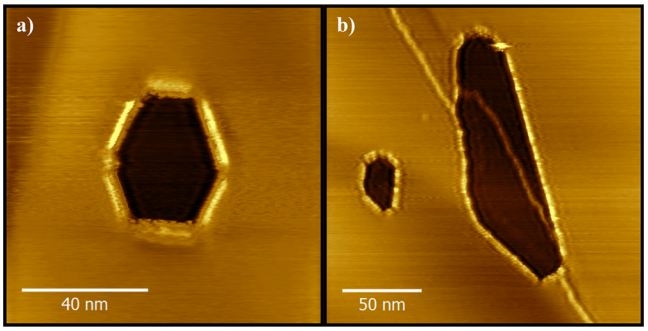

Figure 10. Images of pits on a 1375 K SPI-2 surface exposed to 0.7 eV O_2 impinging at 45° relative to the surface normal. (A) A faceted pit typical of those that dominated the surface. (B) An example of a large, elongated pit that formed on a linear defect. Both images were taken at 100 mV and 600 pA.

CONCLUSION

We have demonstrated the efficacy of using STM and supersonic molecular beams in tandem to combine the realms of macroscopic interfacial kinetics with atomic, nano, and mesoscale morphology, allowing a more holistic examination of graphite oxidation. This novel approach allows us to directly link the time-evolving morphology of the reacting interface with the observed reaction kinetics, in essence, giving access to the spatiotemporal correlations that govern time-evolving interfacial reactivity. The results presented in this paper have uncovered independent effects of oxygen energy, angle, and surface temperature on etching morphology, dictating the formation of hexagonal pits, circular pits, or anisotropic channels. Lower energy (0.4 eV) impinging oxygen produced pits faceted along crystallographic directions on a 1275 K surface that transitioned into circular pits with a 100 K temperature increase. Experiments with different incident angles that compared outcomes using normal versus 45° angles found only limited kinetic and morphological changes. The reaction probability under a given set of experimental conditions remained constant as the etch features evolved, suggesting that the availability of reactive edge carbons is not the limiting factor in the oxidation rate. An increase in oxygen energy from 0.4 to 0.7 eV created anisotropic channels at all surface temperatures, with these features dominating the morphological landscape while other features, such as faceted, circular, and elliptical pits, still exist. Furthermore, the reaction probability increased with impinging oxygen energy, indicating a kinetically distinct process giving rise to the channels. Comparison of the relative reactivity of higher grade versus lower grade HOPG indicates that the formation of etched channels largely depends on the presence of grain boundaries. The fine control over the complete parameter space of surface temperature along with oxygen energy, angle, and flux afforded by this experimental technique has provided fresh insights into the oxidation mechanism for this important model system. Moreover, these findings are of further interest given current needs to perfect advanced carbon-containing materials for high-performance flight, re-entry vehicles, and next generation propulsion systems that need to operate in aggressive oxidizing and high-temperature environments.

AUTHOR INFORMATION

Corresponding Author

*E-mail: s-sibener@uchicago.edu; Phone: 773-702-7193.

ORCID

S. J. Sibener: 0000-0002-5298-5484

Author Contributions

†RE and TG contributed equally to this work and are co-first authors of this manuscript

Notes

The authors declare no competing financial interest.

ACKNOWLEDGMENTS

This work was supported by the National Science Foundation, Grant No. CHE-1566364, with focus on spatio-temporal reaction kinetics. It was also supported by the Air Force Office of Scientific Research, Grant No. FA9550-15-1-0428, with focus on research in support of hypersonic flight. Support from the NSF-Materials Research Science and Engineering Center at the University of Chicago, Grant No. NSF-DMR-14-20709, is also gratefully acknowledged.

REFERENCES

(1) Blyholder, G.; Eyring, H. Kinetics of Graphite Oxidation. *J. Phys. Chem.* **1957**, *61*, 682−688.

(2) Strange, J. F.; Walker, P. L. Carbon-Carbon Dioxide Reaction: Langmuir-Hinshelwood Kinetics at Intermediate Pressures. *Carbon* **1976**, *14*, 345−350.

(3) Marchon, B.; Carrazza, J.; Heinemann, H.; Somorjai, G. A. TPD and XPS Studies of O_2, CO_2, and H_2O Adsorption on Clean Polycrystalline Graphite. *Carbon* **1988**, *26*, 507−514.

(4) Kamioka, I.; Izumi, K.; Kitajima, M.; Kawabe, T.; Ishioka, K.; Nakamura, K. G. Translational Energy Distribution of CO Produced in Infrared-Laser-Assisted Reaction of O_2 with a Graphite Surface. *Jpn. J. Appl. Phys.* **1998**, *37*, L74.

(5) Olander, D. R.; Siekhaus, W.; Jones, R.; Schwarz, J. A. Reactions of Modulated Molecular Beams with Pyrolytic Graphite. I. Oxidation of the Basal Plane. *J. Chem. Phys.* **1972**, *57*, 408−420.

(6) Olander, D. R.; Jones, R. H.; Schwarz, J. A.; Siekhaus, W. J. Reactions of Modulated Molecular Beams with Pyrolytic Graphite. II Oxidation of the Prism Plane. *J. Chem. Phys.* **1972**, *57*, 421−433.

DOI: 10.1021/acs.jpcc.8b04139
J. Phys. Chem. C 2018, 122, 14706−14713

(7) Acharya, T. R.; Olander, D. R. The Rate of Oxidation of the Basal and Prismatic Surfaces of Pyrolytic Graphite in the Transition Regime between Chemical and Diffusional Control. *Carbon* **1973**, *11*, 7−18.
(8) Sun, T.; Yao, X.; Fabris, S. Effects of Thermal Electronic Excitations on the Diffusion of Oxygen Adatoms on Graphene. *J. Phys. Chem. A* **2016**, *120*, 2607−2613.
(9) Chang, H.; Bard, A. J. Scanning Tunneling Microscopy Studies of Carbon-Oxygen Reactions on Highly Oriented Pyrolytic Graphite. *J. Am. Chem. Soc.* **1991**, *113*, 5588−5596.
(10) Chu, X.; Schmidt, L. D. Reactions of NO, O_2, H_2O, and CO_2 with the Basal Plane of Graphite. *Surf. Sci.* **1992**, *268*, 325−332.
(11) Stevens, F.; Kolodny, L. A.; Beebe, T. P. Kinetics of Graphite Oxidation: Monolayer and Multilayer Etch Pits in HOPG Studied by STM. *J. Phys. Chem. B* **1998**, *102*, 10799−10804.
(12) Hahn, J. R. Kinetic Study of Graphite Oxidation Along Two Lattice Directions. *Carbon* **2005**, *43*, 1506−1511.
(13) Xu, S. C.; Chen, H.-L.; Lin, M. C. Quantum Chemical Prediction of Reaction Pathways and Rate Constants for the Reactions of O_x (x = 1 and 2) with Pristine and Defective Graphite (0001). *J. Phys. Chem. C* **2012**, *116*, 1841−1849.
(14) Wiggins, B.; Avila-Bront, L. G.; Edel, R.; Sibener, S. J. Temporally and Spatially Resolved Oxidation of Si(111)-(7 × 7) Using Kinetic Energy Controlled Supersonic Beams in Combination with Scanning Tunneling Microscopy. *J. Phys. Chem. C* **2016**, *120*, 8191−8197.
(15) Hahn, J. R.; Kang, H. Vacancy and Interstitial Defects at Graphite Surfaces: Scanning Tunneling Microscopic Study of the Structure, Electronic Property, and Yield for Ion-Induced Defect Creation. *Phys. Rev. B: Condens. Matter Mater. Phys.* **1999**, *60*, 6007−6017.
(16) Lee, S. M.; Lee, Y. H.; Hwang, Y. G.; Hahn, J. R.; Kang, H. Defect-Induced Oxidation of Graphite. *Phys. Rev. Lett.* **1999**, *82*, 217−220.
(17) Chu, X.; Schmidt, L. D. Gasification of Graphite Studied by Scanning Tunneling Microscopy. *Carbon* **1991**, *29*, 1251−1255.
(18) Atamny, F.; Schlögl, R.; Wirth, W. J.; Stephan, J. Topochemistry of Graphite Oxidation. *Ultramicroscopy* **1992**, *42-44*, 660−667.
(19) Klusek, Z. Scanning Tunneling Microscopy and Spectroscopy of the Thermally Oxidized (0001) Basal Plane of Highly Oriented Pyrolitic Graphite. *Appl. Surf. Sci.* **1998**, *125*, 339−350.
(20) Tandon, D.; Hippo, E. J.; Marsh, H.; Sebok, E. Surface Topography of Oxidized HOPG by Scanning Tunneling Microscopy. *Carbon* **1997**, *35*, 35−44.
(21) Zhu, Y.-J.; Hansen, T. A.; Ammermann, S.; McBride, J. D.; Beebe, T. P. Nanometer-Size Monolayer and Multilayer Molecule Corrals on HOPG: A Depth-Resolved Mechanistic Study by STM. *J. Phys. Chem. B* **2001**, *105*, 7632−7638.
(22) Böttcher, A.; Heil, M.; Stürzl, N.; Jester, S. S.; Malik, S.; Pérez-Willard, F.; Brenner, P.; Gerthsen, D.; Kappes, M. M. Nanostructuring the Graphite Basal Plane by Focused Ion Beam Patterning and Oxygen Etching. *Nanotechnology* **2006**, *17*, 5889.
(23) Paredes, J. I.; Martínez-Alonso, A.; Tascón, J. M. D. Comparative Study of the Air and Oxygen Plasma Oxidation of Highly Oriented Pyrolytic Graphite: A Scanning Tunneling and Atomic Force Microscopy Investigation. *Carbon* **2000**, *38*, 1183−1197.
(24) Murray, V. J.; Marshall, B. C.; Woodburn, P. J.; Minton, T. K. Inelastic and Reactive Scattering Dynamics of Hyperthermal O and O_2 on Hot Vitreous Carbon Surfaces. *J. Phys. Chem. C* **2015**, *119*, 14780−14796.
(25) Murray, V. J.; Smoll, E. J.; Minton, T. K. Dynamics of Graphite Oxidation at High Temperature. *J. Phys. Chem. C* **2018**, *122*, 6602−6617.
(26) Liu, G. N.-K. *High Temperature Oxidation of Graphite by a Dissociated Oxygen Beam*; DTIC Technical Report AD-779−949; Defense Technical Information Center: Fort Belvoir, VA, USA, 1973.
(27) Sun, T.; Fabris, S.; Baroni, S. Surface Precursors and Reaction Mechanisms for the Thermal Reduction of Graphene Basal Surfaces Oxidized by Atomic Oxygen. *J. Phys. Chem. C* **2011**, *115*, 4730−4737.
(28) Poovathingal, S.; Schwartzentruber, T. E.; Srinivasan, S. G.; van Duin, A. C. T. Large Scale Computational Chemistry Modeling of the Oxidation of Highly Oriented Pyrolytic Graphite. *J. Phys. Chem. A* **2013**, *117*, 2692−2703.
(29) Carlsson, J. M.; Hanke, F.; Linic, S.; Scheffler, M. Two-Step Mechanism for Low-Temperature Oxidation of Vacancies in Graphene. *Phys. Rev. Lett.* **2009**, *102*, 166104.
(30) Delehouzé, A.; Rebillat, F.; Weisbecker, P.; Leyssale, J.-M.; Epherre, J.-F.; Labrugère, C.; Vignoles, G. L. Temperature Induced Transition from Hexagonal to Circular Pits in Graphite Oxidation by O_2. *Appl. Phys. Lett.* **2011**, *99*, 044102.
(31) Stevens, F.; Beebe, T. P. Computer Modeling of Graphite Oxidation: Differences Between Monolayer and Multilayer Etching. *Comput. Chem.* **1999**, *23*, 175−183.
(32) Hahn, J. R.; Kang, H.; Song, S.; Jeon, I. C. Observation of Charge Enhancement Induced by Graphite Atomic Vacancy: A Comparative STM and AFM Study. *Phys. Rev. B: Condens. Matter Mater. Phys.* **1996**, *53*, R1725−R1728.
(33) Hembacher, S.; Giessibl, F.; Mannhart, J.; Quate, C. F. Revealing the Hidden Atom in Graphite by Low-Temperature Atomic Force Microscopy. *Proc. Natl. Acad. Sci. U. S. A.* **2003**, *100*, 12539−12542.
(34) Chu, X.; Schmidt, L. D. Intrinsic Rates of Nitrogen Oxide (NO_x)-Carbon Reactions. *Ind. Eng. Chem. Res.* **1993**, *32*, 1359−1366.
(35) Tracz, A.; Wegner, G.; Rabe, J. P. Kinetics of Surface Roughening via Pit Growth During the Oxidation of the Basal Plane of Graphite. 1. *Langmuir* **1993**, *9*, 3033−3038.
(36) Rodriguez-reinoso, F.; Thrower, P. A. Microscopic Studies of Oxidized Highly Oriented Pyrolytic Graphites. *Carbon* **1974**, *12*, 269−279.

DOI: 10.1021/acs.jpcc.8b04139
J. Phys. Chem. C 2018, 122, 14706−14713